JGR Atmospheres

RESEARCH ARTICLE
10.1029/2020JD032858

Special Section:
A NEW ERA OF LIGHTNING OBSERVATIONS FROM SPACE

GLM and ABI Characteristics of Severe and Convective Storms

Kevin C. Thiel[1,2,3], Kristin M. Calhoun[3], Anthony E. Reinhart[3], and Donald R. MacGorman[1,2]

[1]School of Meteorology, University of Oklahoma, Norman, OK, USA, [2]Cooperative Institute for Mesoscale Meteorological Studies, University of Oklahoma, Norman, OK, USA, [3]NOAA/OAR/National Severe Storms Laboratory, Norman, OK, USA

Key Points:
- Areas with cloud tops colder than 240 K typically produce lightning
- Increasing local flash density correlates with decreasing flash areas, higher cloud-top heights, and colder cloud-top temperatures
- The GOES-16 viewing angle to convective features complicates the interpretation of ABI data, especially cloud-top height

Correspondence to:
K. C. Thiel,
kevin.thiel@ou.edu

Citation:
Thiel, K. C., Calhoun, K. M., Reinhart, A. E., & MacGorman, D. R. (2020). GLM and ABI characteristics of severe and convective storms. *Journal of Geophysical Research: Atmospheres*, *125*, e2020JD032858. https://doi.org/10.1029/2020JD032858

Received 31 MAR 2020
Accepted 30 JUN 2020
Accepted article online 3 AUG 2020

Abstract The recent deployment of the Geostationary Lightning Mapper (GLM) on board GOES-16 and GOES-17 provides a new perspective of total lightning production for the severe convective storms research and operational communities. While the GLM has met its performance targets, further understanding flash characteristics and the physical limitations of the GLM are required to increase the applicability of the data. Derived cloud-top height and infrared (IR) brightness temperature products from the Advanced Baseline Imager (ABI) are used to assess data quality and characteristics from gridded GLM imagery across 7 weeks of active severe weather: 13 April through 31 May 2019. Areas with cloud tops colder than 240 K typically produced lightning, though this becomes less certain near the edge of the field of view due to algorithm limitations. Increasing flash rates were observed to correlate with decreasing flash areas, increasing cloud-top heights, and colder cloud-top temperatures. However, flash rates and size were more strongly tied to convective intensity and proximity to convective hazards at the surface due to the ability to delineate between convective and stratiform precipitation. Results show that merging ABI and GLM data sets could add value to both machine learning and statistical-based algorithms and also forecast applications with each providing unique details, although parameters such as GOES-16 viewing angle should be considered. Lastly, two case studies (24 and 27 May 2019) are used to help interpret the results from the 7-week sampling period and identify GLM and ABI trends related to thunderstorm evolution.

Plain Language Summary This study investigates the utility of lightning flash data from the new Geostationary Lightning Mapper (GLM) on the recently launched U.S. weather satellites. Guidance regarding the use of GLM data is needed to improve the quality of forecasts and research, especially when using the data for nonsevere and severe thunderstorms. Comparisons are made between the rate of flashes and their size, along with cloud-top properties from another instrument on the weather satellite, the Advanced Baseline Imager (ABI). Using 7 weeks of data during the peak of the 2019 severe storms season (April and May), we demonstrate that higher lightning flash rates are correlated with smaller-sized flashes as a thunderstorm's cloud top becomes higher and colder. Cloud tops colder than approximately −30°C may also be used to discriminate between regions with and without lightning activity.

1. Introduction

Forecasters and researchers alike benefit from studying atmospheric convection from a variety of observing platforms, which together provide a more accurate and timely perspective of thunderstorm dynamics, kinematics, and microphysics. Some of the most relevant platforms for studying atmospheric convection include radar, satellite, surface weather stations, rawinsondes, lightning location systems (LLS), and human observers. Geostationary observations via satellite have provided the ability to monitor and study convection over vast spatial domains (thousands of km), since the initial launch of the first Geostationary Operational Environmental Satellite (GOES) in 1975. This effort has been furthered with the launch of the GOES R-Series in November 2016. The two Earth-facing instruments on GOES-16 and GOES-17, the Advanced Baseline Imager (ABI) (Schmit et al., 2017) and the Geostationary Lightning Mapper (GLM) (Goodman et al., 2013), provide an increased ability to monitor convection at finer spatial and temporal scales, along with new products leading to expanded user applications and research involving atmospheric convection.

©2020. American Geophysical Union. All Rights Reserved. This article has been contributed to by US Government employees and their work is in the public domain in the USA.

Geostationary radiance measurements with frequencies from the visible to infrared (IR) ranges have long been used by the U.S. National Weather Service (NWS) and the severe storms research community. Rapid temporal and spatial changes in the optical radiance of cloud tops or their brightness temperatures allow for approximations of the geometric and microphysical characteristics of convection. Direct convective applications of visible and IR satellite data include observations of cloud-top phenomena associated with the initiation of convection (Purdom, 1976; Roberts & Rutledge, 2003) and the potential for severe weather such as the overshooting tops of convective updrafts (Solomon et al., 2016). However, the ability to observe cloud-top radiances and total lightning production from a single observing platform provides a unique opportunity to study flashes relative to their cloud-top characteristics from both a severe storms research and operational forecast perspective.

While lightning is its own public hazard (Curran et al., 2000; Jensenius, 2019), lightning data in the context of thunderstorms provide insight into the kinematic and microphysical processes that govern storm morphology (Darden et al., 2010; MacGorman et al., 1981; Mecikalski & Carey, 2018; Schultz et al., 2015; Schmit et al., 2017; Williams et al., 1999). Noninductive charge separation within the mixed-phase region of a convective updraft (Calhoun et al., 2013, 2014; Emersic & Saunders, 2010; Mansell et al., 2005; Takahashi, 1978; Ziegler & MacGorman, 1994) followed by sedimentation and thunderstorm kinematics drives the organization of these charged particles into layers or regions of homogeneous charge. Lightning flashes initiate between two opposing regions of charge (MacGorman et al., 1981; MacGorman & Rust, 1998; Williams, 1985), and the convective nature of the storm therefore controls the areal extent of individual flashes (Bruning & MacGorman, 2013). More specifically, forecasters can use substantial increases in flash rates before severe weather phenomena such as large hail, damaging winds, or tornadoes known as lightning jumps to detect significant changes to a storm's kinematic behavior (Schultz et al., 2009; Williams et al., 1999). Changes to updraft characteristics (e.g., updraft speed and width) occur as a convective updraft strengthens, leading to variations of vertical velocities near the updraft regime, creating areas of small, yet concentrated, regions of charge (Schultz et al., 2015, 2017). This process promotes increasing flash rates with decreasing flash size in close proximity to the convective updraft, as previously noted by Bruning and MacGorman (2013), resulting in greater local flash extent density (FED) in more turbulent regions and lower FED in more stratified regions of convective storms.

The GLM was designed with a detection efficiency (DE) of >70% and a false alarm rate (FAR) of <5%; however, the DE of flashes within severe and local storms has come into question, suggesting that the optical depth of the storm may lead to reduced flash counts among the smallest, least luminous flashes (Calhoun et al., 2018). Flash DE and FAR from the GLM have also been shown to vary spatially and temporally (Bateman & Mach, 2020), and as a function of viewing angle relative to the satellite (Murphy & Said, 2020), with the angles furthest from the satellite subject to decreased DE. In order to increase the operational and research applicability of GLM data, further investigations of the GLM relative to other geostationary platforms such as the ABI are needed. This study utilizes gridded GLM and ABI data sets to investigate nonsevere and severe deep, moist convection observed by GOES-16. Spatially, variables are studied with respect to viewing angle to further understand the geometric effects imparted on both instruments and their products. Lastly, case studies of two differing convective modes are used to interpret thunderstorm morphology in the context of GLM and ABI variables.

2. Data and Methods

2.1. ABI

The ABI (Schmit et al., 2017) is a 16-band radiometer that covers the visible, near-IR, and IR wavelengths between 0.47 and 13.3 μm and has resolutions at the satellite subpoint between 0.5 and 2 km. The ABI provides measurements for a vast majority of the Western Hemisphere in the midlatitude and tropical regions with one full disk, one continental United States (CONUS), and two floating mesoscale scenes. Measured radiances from each band are the building blocks for a variety of ABI-derived products related to atmospheric composition, convection, and kinematics.

Two ABI Level-2 algorithms are utilized to provide a physical reference of thunderstorm attributes and intensity with respect to the GLM: the ABI cloud-top height algorithm (ACHA) (Heidinger, 2013) and the Cloud Moisture Imagery Product (CMIP) (Schmit et al., 2012). In order to generate the CMIP data, radiances from each of the 16 ABI bands are first converted to spectral radiances, followed by a second conversion

to reflectance factors for the six visible and near-IR bands, and brightness temperatures for the remaining 10 IR bands. Reflectance factor and brightness temperature from the CMIP are then used to build other L2 products such as the ABI clear-sky mask (ACM), ABI cloud-top type (ACT), and the ACHA. Brightness temperatures from band 13 at 10.3 μm are used with the ACM applied to infer cloud-top brightness temperatures in convective environments. Band 13 is referred to as the "clean" longwave IR band due to reduced absorption of ambient water vapor and ozone, providing a more accurate picture of convective updraft intensity and glaciation rates at a resolution of 2 km (1,500 by 2,500 pixels across the CONUS domain).

The ACHA uses CMIP data from IR bands 14, 15, and 16 (11.2, 12.3, and 13.3 μm), ACT, and numerical weather prediction (NWP) data from the Global Foreacast System (GFS) to generate cloud-top height, temperature, and pressure for all cloudy pixels defined by the ACM. The collection of ABI and NWP data was used along with blackbody radiance profiles and clear-sky estimates to determine top of atmosphere radiances and therefore calculate cloud-top temperature at a resolution of 2 km. Cloud-top temperatures are then compared against vertical profiles from the GFS to determine cloud-top height and pressure at horizontal resolutions of 10 km (300 by 500 pixels across the CONUS domain). For the purpose of this study, cloud-top heights are used to provide a reference for cloud depth and to monitor the development of convection.

2.2. GLM

The GLM (Goodman et al., 2013) is the first optical instrument to detect lightning continuously over a near hemispheric field of view. While ground-based networks use a series of instruments to detect and measure the electromagnetic radiation from flashes (Cummins & Murphy, 2009), the GLM is a single instrument that detects rapid optical changes in energy at the 777.4-nm wavelength with a 2-ms frame rate. This is accomplished by using a narrowband interference filter on a high-speed charge-coupled device (CCD) focal plane. Resolution of GLM pixels varies from 8 km at nadir to 14 km at the edge of the field of view. Pixels which exceed their previously measured background energy threshold by approximately 4.5 standard deviations in a single time frame are recorded as events, which serve as the fundamental unit of GLM data. From these GLM events, higher-order tiers of data are constructed using the GLM Lightning Cluster Filter Algorithm (LCFA) (Goodman et al., 2012). Adjacent events within the same frame are classified as groups and clustered spatially and temporally into flashes with thresholds of 16.5 km and 330 ms, respectively. Performance specifications of the GLM include a 24-hr average flash DE of greater than 70% and FAR of less than 5%.

While false events detected by the GLM are often removed during ground processing, more complex artifacts still remain. Features such as Sun glint off of bodies of water, small miscalibrations at CCD subarray boundaries, solar intrusions during the eclipse seasons, and satellite jitter can all contribute to false clusters of events, and therefore false flashes, being included in the GLM data (Rudlosky et al., 2019). A majority of these false events have been filtered out by updates in ground processing as of 25 July 2019 (Edgington, 2020; Rudlosky & Armstrong, 2019). In order to minimize data latency of the GLM data for real-time analysis by forecasters, the LCFA also has defined limits on the number of events within a group and the number of groups within a flash, which has been found to degrade over 3% of all GLM flashes (Peterson, 2019).

In order to improve operational application of the GLM, gridded GLM imagery has been developed to quantify the areal coverage, frequency, and intensity of recorded lightning flashes as an open-source software package, glmtools (Bruning, 2019; Bruning et al., 2019). glmtools uses parent-child relationships between event, group, and flash data produced by the GLM LCFA to recreate the areal extent of flashes and groups native to the instrument spatial detection capabilities, and outputting to the same fixed grids used by the ABI at a resolution of 2 km (1,500 by 2,500 pixels across the CONUS domain). Products are then accumulated over a 1-min interval for each variable. The products from glmtools are now available to a variety of operational users through experimental feeds and have undergone testing by NWS forecasters at the NWS Hazardous Weather Testbed (HWT) during May of 2018 and 2019 in Norman, Oklahoma (Calhoun, 2018; 2019). When used in tandem with other satellite and radar products, the gridded GLM imagery was noted to increase forecaster confidence in monitoring and predicting severe convection. The products most useful for forecasters included FED, total optical energy (TOE), minimum flash area (MFA), and event density (ED), with 5-min product accumulations updating each minute reported as the primary tool for monitoring changes in flash characteristics and thunderstorm severity.

Two products created by glmtools from the GLM are used to understand the changing flash characteristics of convection with respect to convective intensity, FED and MFA. FED represents the total number of unique flashes that propagate through a given pixel over a 1-min time period, to provide a spatial projection of the

frequency of flashes. Respectively, MFA represents the minimum value of all calculated flash areas that pass through the pixel to provide context for the physical characteristics of the flashes.

2.3. Data Collection and Processing

Between 13 April and 31 May 2019, GLM and ABI data from GOES-16 were investigated to compare flash products from the GLM to derived ABI products. This period was chosen due to several significant severe weather events that produced a large number of hail, wind, and tornado local storm reports (LSRs). Also, a variety of storm modes occurred across the central and eastern United States, including discrete, single cell convection, supercells, stratiform precipitation, and quasi-linear convective systems (QLCSs). Because convective mode and intensity can substantially alter the frequency and size of flashes as previously discussed, a large-scale sampling approach across the CONUS provides a robust assessment of the ABI and GLM for severe and nonsevere storms.

The GLM variables are accumulated over a 5-min window that coincides with the ABI product output frequency in Mode 6 (Super Flex). Accumulation of FED are made every 5 min, along with selecting the minimum, nonzero MFA value for each grid cell. This study utilizes a 2-km horizontal resolution to match the operational GLM products currently being used and developed for NWS forecasters. However, considerable differences in resolution between the gridded GLM products, the GLM native resolution, and the lower-resolution ABI products exist; therefore, a selective sampling method is employed to fit these observations to one grid and ensure the values observed can be applied operationally. The 2-km GLM gridded products are accumulated into 20-km cells across the entire domain (10 pixels by 10 pixels) with the maximum value of FED and minimum MFA value assigned to the center point of each new 20-km pixel (150 by 250 pixels across the CONUS domain). Both ABI products have also been selectively sampled to the same 20-km grid as the GLM data, utilizing the maximum cloud-top height and minimum cloud-top brightness temperature within the 20-km sampling region. With all ABI and GLM products now on the same selectively sampled grid and matching temporal frequency, point-by-point comparisons between the GLM and ABI-derived variables can be made in order to provide greater physical context for the cloud tops from which GLM flashes are emitted.

In order to subset the GLM and ABI data with respect to the strongest convective storms, grid points are identified based upon their spatial and temporal proximity to LSRs related to hail exceeding 25 mm (1 in.), thunderstorm wind gusts over 25 m s^{-1} (58 mph), observed thunderstorm wind damage, and tornadoes. Incorporating LSRs into the data set provides additional context for the ABI and GLM observations but comes with caveats carried by the LSR database. Both hail and wind LSRs face issues related to the number of reports and biases in their reporting (Allen & Tippett, 2015; Kelly et al., 1985; Trapp et al., 2006). Allen and Tippett (2015) and Trapp et al. (2006) pointed out that the number of reports for each event does not adequately represent their respective magnitudes or damages. Along with the constraint of hail and wind reports to cities and major roads, which was frequently observed during the 7-week study, the presence of other "more spectacular" phenomena such as tornadoes can also take prominence in reporting (Kelly et al., 1985). Even though tornado LSRs are one of the best-kept records since the formal adoption of the Fujita scale in 1975, only approximately 45% of tornadoes have been reported (Potvin et al., 2019). With respect to the ABI and GLM CONUS sectors, LSRs are also limited to land-based observations over the United States so other storms producing severe phenomena outside of this domain are also not included. To minimize the spatial and temporal errors previously described, a K-D tree using a nearest neighbor approach is used to flag the nine closest 20-km grid cells to the desired LSRs ±5 min from each report. All flagged grid cells are accumulated in a binary format, to avoid counting the same data point more than once. This approach also ensures an approximate 30-km sampling radius around each report, ensuring that the ground-based LSRs capture their respective cloud tops regardless of differences in parallax for the ABI-GLM data set (Bruning et al., 2019).

The viewing angle elevation for all cells on the 20-km grid are calculated to assess data characteristics from the ABI and GLM spatially using a spherical-Earth approach described in Soler and Eisemann (1994). While Soler and Eisemann (1994) recommend using an ellipsoidal approach versus the spherical-Earth approach, this only incurs a small improvement (0.02°) at most in the calculation and is still well suited for this study. Viewing angle elevations from GOES-16 range from over 70° across the Caribbean Sea to below 20° in the extreme Pacific Northwest (Figure 1a).

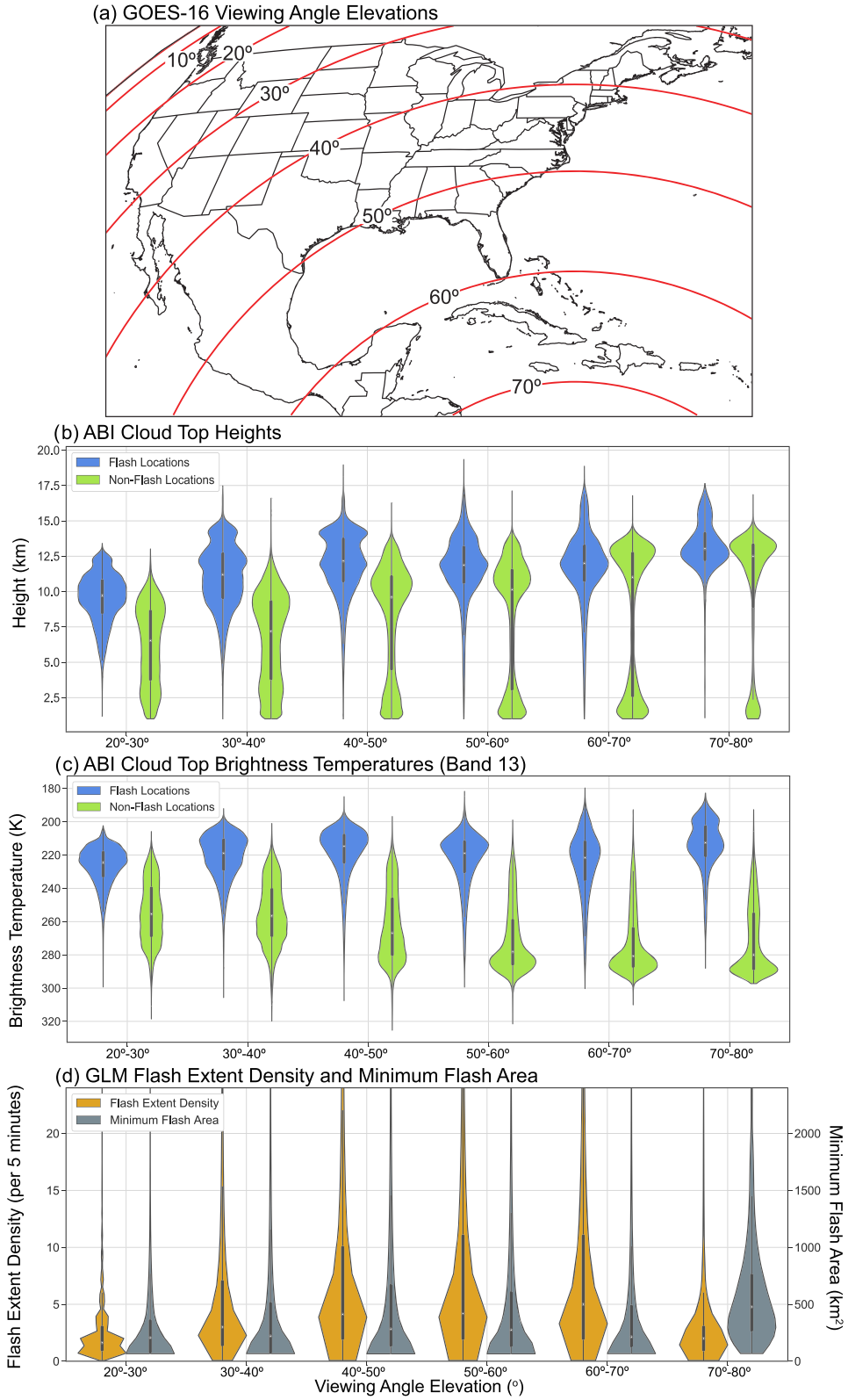

Figure 1. (a) Calculated viewing angle elevations (deg) from GOES-16. Contoured lines are every 10° beginning with 70° closest to nadir. (b) Violin plots of ABI cloud-top heights and (c) ABI clean-IR cloud-top brightness temperatures with an inverted *y* axis binned as a function of viewing angle elevation. Blue violins represent flash locations, and green violins represent nonflash locations. (d) GLM flash extent density (orange) and minimum flash area (gray) binned similar to panels (b) and (c).

2.4. Data Filtering

While the selective sampling method employed above largely mitigates differences in the horizontal resolution between the selected ABI and GLM products, further filtering of the multisensor data set is made to ensure the removal of this effect and artifacts mentioned by Rudlosky et al. (2019). The lower spatial resolution of the ABI cloud-top heights on the edge of convective updrafts has been found to create rapid changes in height from the anvil region to adjacent cumulus clouds over the horizontal span of less than 2 km. With higher flash rates commonly found upshear of the updraft (Bruning & MacGorman, 2013), this can create instances of relatively high flash rates with exceptionally low cloud-top height; therefore, all data points with cloud-top heights below 1 km are considered clear air and removed from the data set.

False GLM events at the boundaries between subarrays east of the Bahamas were also noted by Rudlosky et al. (2019) and observed in this study with exceptionally high flash rates paired with low, warm cloud tops. Across all convective modes, flashes have been found to initiate most often at altitudes between 8 and 12 km (Mecikalski & Carey, 2018), with very few flashes originating below 4 km. For a thunderstorm to maintain consistent charge separation and therefore nominal flash rates, a persistent updraft must be present to lift hydrometeors into the mixed-phase region. Through the charging mechanism previous described by Emersic and Saunders (2010) and Takahashi (1978), cloud-top heights must be above the freezing level and brightness temperatures well below freezing. In response, a second filter was applied to the data set that removes pixels that meet all three of these conditions: (1) cloud-top temperatures warmer than 270 K, (2) cloud-top heights less than 4 km, and (3) FED values exceeding 10 flashes per 5 min.

3. Results

3.1. Cloud-Top Characteristics of Flashes

Through the 7-week study, 604.8 million selectively sampled grid cells were recorded, with over 4.6 million cells containing both GLM and ABI data with flashes observed over a variety of cloud-top heights and brightness temperatures (clean IR-brightness temperatures will be referred to as just brightness temperatures hereafter). The distribution of these points was compared against 2 million randomly sampled points that did not contain GLM flashes but did contain ABI cloud-top data and binned as a function of viewing angle elevation every 10° from the surface for both cloud-top heights and brightness temperatures (Figures 1b and 1c). Sample sizes of the distributions for the number of grid cells containing GLM flashes from the 20–30° bin to the 70–80° bin were 169373, 704340, 1750569, 1068649, 919480, and 5963 unique locations. The respective sample size of nonflash locations was 185729, 498431, 568718, 376499, 322245, and 39110.

The interquartile ranges of cloud-top heights containing GLM flashes were typically between 10 and 13 km regardless of viewing angle elevation (Figure 1b). Cloud-top heights without lightning featured varying interquartile ranges from as low as 2.5 km to higher than 13 km, driven by peaks in their frequency often at these heights. Less overlap of the interquartile ranges of each group does exist at smaller viewing angle elevations. Cloud-top heights with lightning exceeding the 90th percentile of each distribution exceed 17 km, while their corresponding 10th percentile of heights between 5 and 7 km. The distributions without GLM data show 90th percentile heights up to 3 km lower than those with lightning, with a strong clustering of the 10th percentile heights between 1 and 3 km. Cloud tops containing flashes in the 20–30° and 30–40° look angle bins reflect lower cloud-top heights, especially so in the 20–30° bin. In comparison to the binned distributions where ABI data were present but there were no observed GLM flashes, the 20–30° and 30–40° bins also show decreasing heights at their 90th percentile heights. The nonflash distributions also shift from a near-uniform distribution of recorded heights with the 20–30° and 30–40° bins to a bimodal distribution with increasing viewing angle elevation, leading to a clustering of heights below 4 km and above 8 km based upon peaks in their respective kernel densities. Also, as the viewing angle increases for the height distributions without lightning, the median and 75th percentile values for each bin approach the corresponding values of the height distributions with GLM flashes, eventually by less than 1 km at the 70–80° bin.

With respect to the cloud-top brightness temperature distributions, all interquartile ranges containing lightning as detected from the GLM featured temperatures colder than 240 K, with median values around 220 K (Figure 1c). These median values are up to 60 K colder when compared against the cloud tops without GLM data, with all inner-quartile ranges of these distributions warmer than 240 K. Within the distributions without lightning, there was also a notable shift in temperatures above and below viewing angles of 40°, with the distributions of nonlightning producing clouds at viewing angles greater than 40° displaying a stronger bias

toward warmer cloud-top temperatures (median values closer to 280 K) while those below 40° are marked with more normal distributions (median values near 250 K). The differences between the two distributions for each bin were most apparent for satellite viewing angle elevations greater than 40°, implying that clouds with updrafts and cooling rates clearly supportive of electrification (less than 240 K) are more distinct when compared to cloud-top brightness temperatures in regions where satellite viewing angles are less than 40°.

Distributions of GLM FED and MFA also show variations as a function of viewing angle (Figure 1d). Median FED counts for viewing angle elevations between 40° and 70° were between four and five flashes per 5 min, with bins below 40° and above 70° at lower counts of one and three flashes per 5 min. The variation between these two groups was even greater at the 75th percentile, with values from 10 to 11 and 3 to 7 flashes per 5 min, respectively. Median MFA sizes were consistently between 206 and 282 km^2 for all viewing angle elevations from 20° to 70°. However, the 70° to 80° bin had a median MFA size of 477 km^2 and was more than twice the size of three other bins. The 70° to 80° bin also had the largest MFA at the 75th percentile (755 km^2), with all other bins between 354 and 664 km^2.

3.2. ABI-GLM Relationships

GLM flashes occurred at a variety of cloud-top heights and brightness temperatures throughout this study; therefore, these distributions provide an opportunity to assess how variations in ABI products related to thunderstorm intensity and mode represent changes in GLM flash characteristics (Figure 2). Cloud-top height and brightness temperature show an inverse relationship when examining the axis of higher-density bins (counts greater than 4,000) in Figure 2a. This region of higher-frequency flashes commonly occurred with representative heights (temperatures) above 10 km (colder than 230 K), with a maximum in frequency around 12 km (215 K), similar to observations from Figures 1b and 1c. The inverse height-temperature relationship then continues until the maximum cloud-top heights around 18 km and minimum cloud temperatures around 180 K. Above 13 km, the increasing spread in cloud-top heights with increasing brightness temperature rapidly drops. Below 13 km, however, there is a notably wide spread of very low frequency flashes (counts less than 500) associated with high cloud-top heights and warmer temperatures. This subsection of the distribution deviates considerably from the inverse relationship previously described.

In order to make direct comparisons between the ABI variables and the individual GLM gridded products, three-dimensional scatter plots were created (Figures 2b–2d). These plots include 1,000 randomly sampled points from the original population, with the size of each dot representative of the relative magnitude of a selected GLM variable (greater or fewer FED and larger or smaller MFA). Greater FED values are clustered within the highest cloud tops (above 10 km) and coldest brightness temperatures (below 230 K), signifying that the deepest convective updrafts with the highest rates of glaciation consistently produce the most-prolific flash rates (Figure 2b). At the highest and coldest cloud tops, where greater FED values were found in Figure 2b, MFA values shrunk to less than 200 km^2 (Figure 2c). Conversely, flashes with cloud-top heights below 12 km and brightness temperatures above 220 K grow to larger MFA values (>1,000 km^2) and fewer FED values (<10 per 5 min). The highest density of points in Figures 2b and 2c coincides with the region of highest flash densities in Figure 2a, supporting the points as a representative sample of the overall distribution.

The inverse relationship between MFA and FED as a function of cloud-top height and brightness temperature displays variations in flash characteristics near the thunderstorm updraft. High (>12 km), cold (<220 K) cloud tops contain greater FED (>50 flashes per 5 min) with smaller MFA (<200 km^2) versus the flashes that propagate through the warmer regions of stratified precipitation, with fewer FED and larger MFA. The presence of deep, moist updrafts that loft hydrometeors into the mixed phase region for efficient charge separation can be noted by greater values of FED. Therefore, only the points when FED exceeds the 90th percentile (24 flashes per 5 min) are used in Figure 2d. With the sample containing high flash rates, MFA values were much smaller in comparison to Figure 2c, with nearly all points containing the smallest possible GLM flashes (less than 100 km^2). A shift in the lower bound of the high-density point region to 12 km and 220 K (Figure 2d) also indicates higher cloud-top heights and colder brightness temperatures coincident with these FED values.

Three-dimensional scatter plots from Figure 2 allow for an investigation of direct GLM variable interrelationships in context of the ABI and its ties to thunderstorm morphology. This, however, comes at the cost of a dramatically reduced sample size that is approximately 0.02% of the original population. Also, the high frequency of points in the higher-density region identified in Figure 2a makes identifying definitive

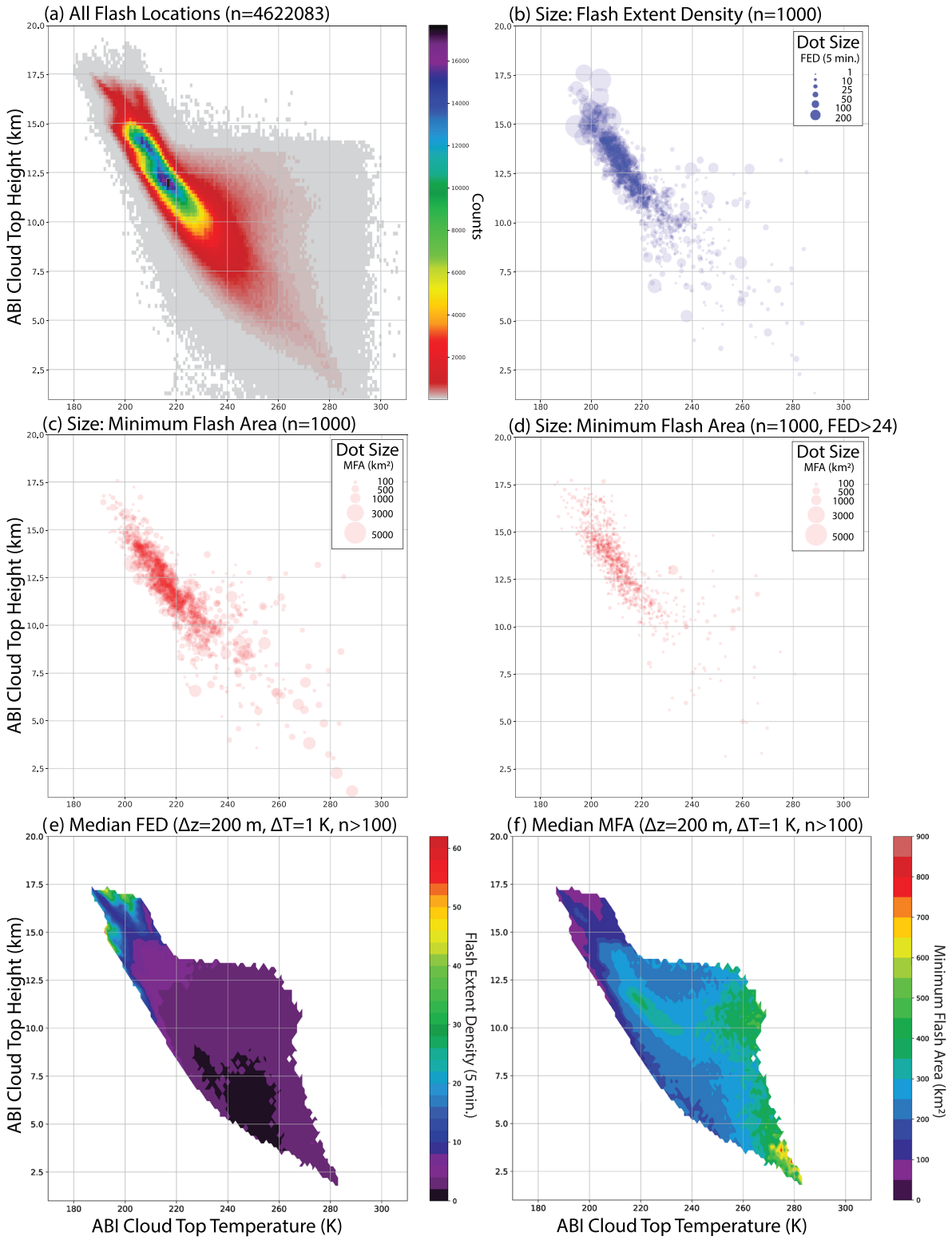

Figure 2. The relationships between the various ABI and GLM variables in the study. Panel (a) represents a 2-D histogram between all cloud-top height and brightness temperature observations at all GLM flash locations. Cloud-top heights were binned every 200 m and brightness temperatures every 1 K. Panels (b) and (c) are 3-D scatter plots, which represent 1,000 randomly sampled FED and MFA values from the population in panel (a), respectively. Panel (d) is similar to panel (c) but is sampled from points with FED values above the 90th percentile (24 flashes per 5 min). Median values of FED (panel e) and MFA (panel f) as a function of their associated height and brightness temperature. Bins were divided every 200 m and 1 K, with median values only sampled from bins with greater than 100 samples.

GLM variable characteristics as a function of cloud-top height and brightness temperature more difficult. To ensure the robustness of the previously defined inverse relationship of FED and MFA, both variables were binned as a function of their corresponding cloud-top heights and brightness temperatures similar to the two-dimensional histogram in Figure 2a. Next, the median FED and MFA values were sampled from each bin with counts greater than 100 (Figures 2d and 2e).

The median FED values in Figure 2d displayed the fewest FED between cloud-top temperatures of 230 and 260 K and heights below 9 km, with FED less than two flashes per 5 min. With higher and colder cloud tops from this minima in FED, the median FED gradually increases. Median FED values between four and eight flashes per 5 min are observed throughout the high-density region identified in Figure 2a, with median FED values above 10 flashes per 5 min sampled at approximate cloud-top brightness temperatures below 200 K or heights above 15 km. This region of greater median FED corresponds with the reduction of sample size again observed in Figure 2a, indicating the rarity for convective cloud tops to obtain brightness temperatures colder than 200 K and heights above 15 km, but in those cases median FED values can increase to greater than 30 flashes per 5 min.

In contrast to the median FED values, the binned median MFA values (Figure 2e) at lower cloud-top heights and warmer cloud-top brightness temperatures did display larger MFA values (200–300 km^2) when compared against the lowest and highest cloud tops. However, MFA values larger than 400 km^2 were consistently sampled at brightness temperatures greater than 260 K and in some cases with cloud tops as cold as 250 K with cloud-top heights between 8 and 12 km. Another peak in the median MFA (300–400 km^2) was present between cloud-top heights of 9 and 12 km and brightness temperatures between 215 and 235 K, before values decreased below 200 km^2 and cloud-top heights increased above 14 km and brightness temperatures below 205 K. Similar to Figure 2d, the region of smaller median MFA corresponds to a reduction in sample size and the increasing rarity of convective updrafts able to produce these values. During these scenarios with more robust updrafts, noted by increasing cloud-top height and decreasing brightness temperature, greater FED values with smaller MFA values are more frequently observed. The observations from Figures 2d and 2e therefore further support those made previously in Figures 2b–2d.

3.3. ABI-GLM Relationships Relative to Severe Local Storms

When subsampling the total population using the data points flagged for their proximity to all 9,509 LSRs, ABI-GLM relationships are studied in the context relative to severe thunderstorms producing impactful hazards at the surface (Figure 3). The higher-frequency (counts greater than 100) range of heights and temperatures containing lightning was above 11 km and below 220 K, with maximum values exceeding 17 km. These values are 1 km higher and 10 K colder when compared against total population in Figure 2a. Also, there are fewer low-density bins exhibiting warm cloud-top brightness temperatures and high cloud-top heights below 13 km, with more values following the inverse cloud-top height and temperature relationship previously described. While Figure 3a does not contain all of the highest cloud-top heights or coldest cloud-top temperatures when compared to the total population observed in Figure 2a, a second axis of values was noted between 200 and 210 K and above 16 km. In this region, the cloud-top heights appeared to rise faster than the generalized cooling rate below 16 km.

When examining variations of FED values as a function of the cloud-top heights and brightness temperatures (Figures 3b and 3d), the greatest FEDs are even more concentrated among the highest and coldest cloud tops compared to Figures 2b and 2d. While diagnosing the distribution of FED values at the most frequent heights and brightness temperatures from Figure 3b is more difficult due to a more obscure clustering of values, the median sampled values from each bin in Figure 3d indicate a distribution that favors more prolific flash rates and therefore larger dot sizes. Similarly, the MFA values are smaller in the higher-density core from Figures 3c and 3e, allowing these points to be more easily observed. Points containing larger MFA values are observed with cloud-top brightness temperatures above 220 K and heights between 6 and 13 km. Because Figures 3b and 3c were both drawn from the same sample size, they can also be analyzed in concert. The greatest (fewest) FED values were strongly correlated with the smallest (largest) MFA values. Similarly, Figures 3d and 3e show a transition from median FED less than 10 per 5 min and MFA greater than 200 km^2 at lower and warmer cloud tops to much greater FED and smaller MFA at cloud-top heights above 13 km and temperatures below 220 K. This again supports the inverse relationship between local lightning flash density and size.

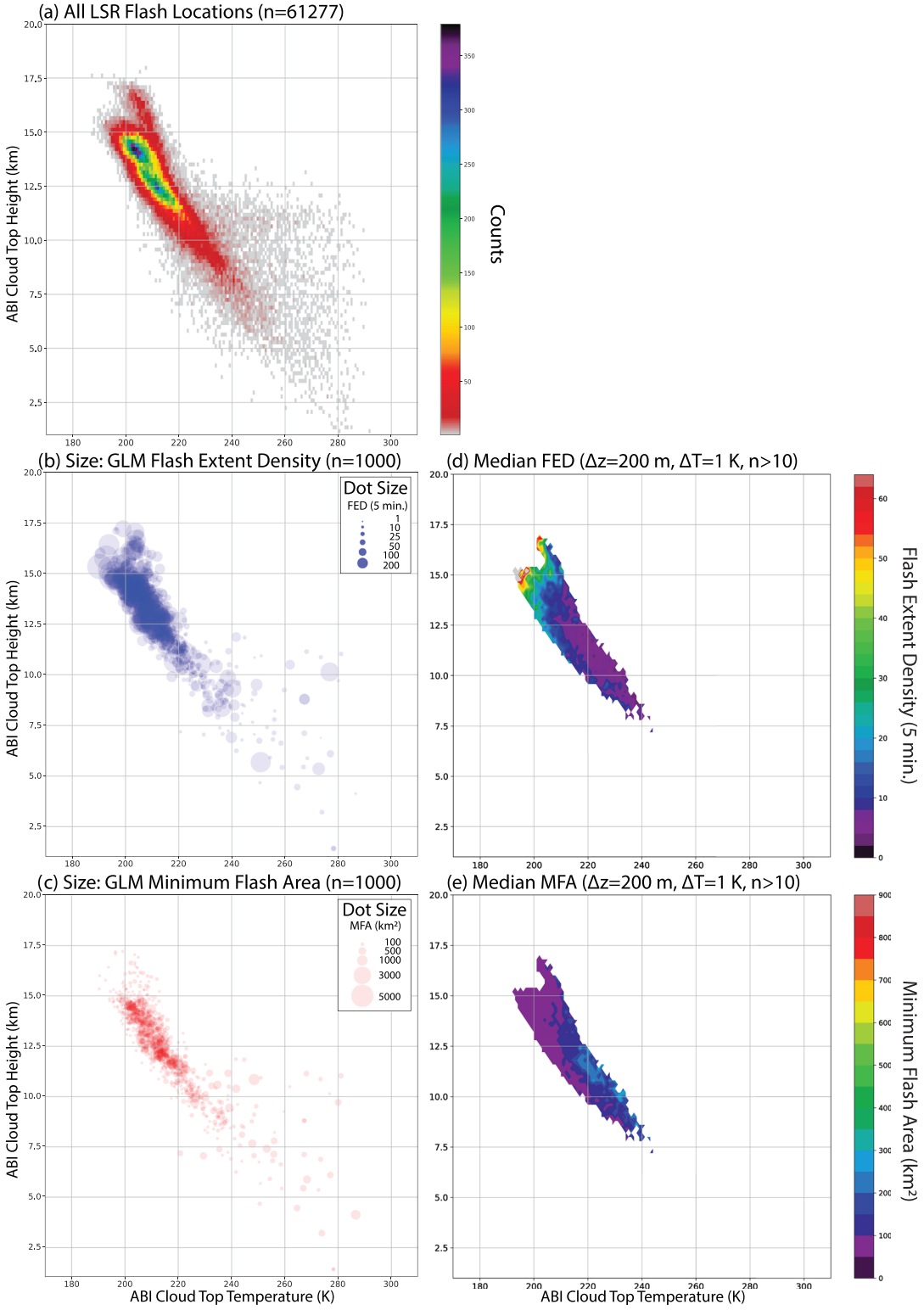

Figure 3. The relationships between the various ABI and GLM variables in the study near local storm reports. Panel (a) represents a 2-D histogram between all cloud-top height and brightness temperature observations at all GLM flash locations. Panels (b) and (c) are 3-D scatter plots that represent 1,000 randomly sampled FED and MFA values from the population in panel (a), respectively. Median values of FED (panel d) and MFA (panel e) were also binned as a function of their associated height and brightness temperature near local storm reports, and divided every 200 m and 1 K. Median values were only sampled from bins with greater than 10 samples.

3.4. Storm-Scale Observations

Two cases of severe convection from the 7-week data set are investigated below to provide context for the codevelopment of ABI and GLM features. First, timing of CI, growth to mature phase, and decay of a supercell storm from 24 May 2019 is reviewed. Next, the growth and maturity of QLCS that developed into a large-scale bowing line as it moved across the central plains overnight on 26–27 May 2019 is covered. Both cases occurred in close geographic proximity, providing a similar viewing angle and removing seasonal variations of storm characteristics. Five-minute GLM composites are used to identify convective trends as noted in Calhoun (2018) and Calhoun (2019), with their original 2-km resolution. ABI cloud-top heights at 10 km and the native resolution of the clean-IR brightness temperatures at 2 km are provided for comparison to the bulk statistics above. Multi-Radar Multi-Sensor (MRMS) (Smith et al., 2016) reflectivity at lowest altitude (RALA) product is also used as a ground-based reference for the convective observations at cloud top and to provide a more complete view of the convection. Lastly, the observed GLM and ABI values were compared against percentiles from their respective total distributions to identify their overall significance.

3.4.1. Supercell Case - 24 May 2019

On 24 May 2019, a deep, longwave trough stretched across the western United States, with subsequent ridging extending eastward across the Great Lakes, and a moist, unstable boundary layer along a stalled frontal boundary across the Texas panhandle into northeast Kansas provided the setup for development of severe storms including supercells. The front acted as a persistent source of lift and destabilization through the afternoon, as surface dew points exceeding 21°C were advected northward into southeast Kansas. Soundings from NWS Norman, OK, and NWS Springfield, MO, at 1200 UTC on 24 May revealed profiles with 40- to 50-kt effective bulk shear supportive of supercell storms. By 1700 UTC, surface-based convection was ongoing in the weakly capped environment across north central Oklahoma and south central Kansas and began moving to the northeast.

Convective initiation of the supercell storm of interest (see storm enclosed by black circle in Figure 4) occurred just after 2000 UTC, indicated by MRMS RALA values greater than 35 dBZ in southern Sumner County Kansas, just north of the Kansas and Oklahoma border. Corresponding to CI, maximum cloud-top heights rose from 11.5 to 14.0 km from 2000 to 2020 UTC, while brightness temperatures decreased from 221 to 206 K in the same period (Figure 5b). Maximum FED values at 2000 UTC (18 flashes per 5 min) were lower when compared to ongoing convection nearby (Figure 5a). Over the proceeding 40 min (until 2040 UTC; Figures 4a–4e), the updraft continued to strengthen with increased MRMS RALA values above 50 dBZ, FED near the updraft increased to 123 flashes over 5 min, and MFA fell below 353 km^2 (Figures 4a–4c). FED values at 2040 UTC exceeded the 99th percentile of all sampled FED in the study, with MFA values still above their respective 60th percentile. Maximum cloud-top heights rose to 15.4 km with minimum brightness temperatures of 203 K (Figures 4d and 4e), which were at the 97th and 7th percentiles, respectively, of all sampled heights and brightness temperatures. During this time, the thunderstorm also began to move right of the mean storm motions from nearby convection after 2040 UTC, along with the development of classic hook-echo signature from MRMS RALA by 2050 UTC, signaling the presence of a maturing mesocyclone inherent with supercell storms.

By 2100 UTC, FED and MFA were holding their respective values from 2040 UTC; however, maximum cloud-top heights now exceeded 16.7 km and cloud-top brightness temperatures of 200 K. These maximum height and minimum brightness temperature ABI values were now exceeding the 99th and 3rd percentiles. Compared to other thunderstorms in the area, the magnitudes of both the ABI and GLM variables show that this supercell storm contained the most robust updraft and organized structure and had the highest potential for severe weather. During the proceeding 15 min from 2100 UTC MFA sizes shrunk to just 70 km^2, indicating that flashes of only one GLM pixel were being recorded and placing this variable below the 20th percentile of all sampled MFA values. By the 2120 UTC time interval (Figures 4f–4j), the supercell storm had two tornado reports and two reports of wind damage at 2119 UTC and featured FED counts exceeding 106 flashes over a 5-min period, MFA sizes of 141 km^2, cloud-top heights of 16.4 km, and cloud-top brightness temperatures above 198 K. FED and MFA continued to stay at their respective magnitudes as the supercell storm continued northeastward, producing a report of severe hail at 2140 UTC, two more reports of wind damage at 2147 and 2150 UTC, and another tornado LSR at 2153 UTC. From 2200 to 2220 UTC, maximum FED counts decreased from its consistent peak of over 100 flashes per 5 min to 58 flashes per 5 min; meanwhile, the region of MFA increased to 356 km^2. MRMS RALA during this period showed widespread convection developing to the north and southeast of the weakening supercell storm, eventually coalescing

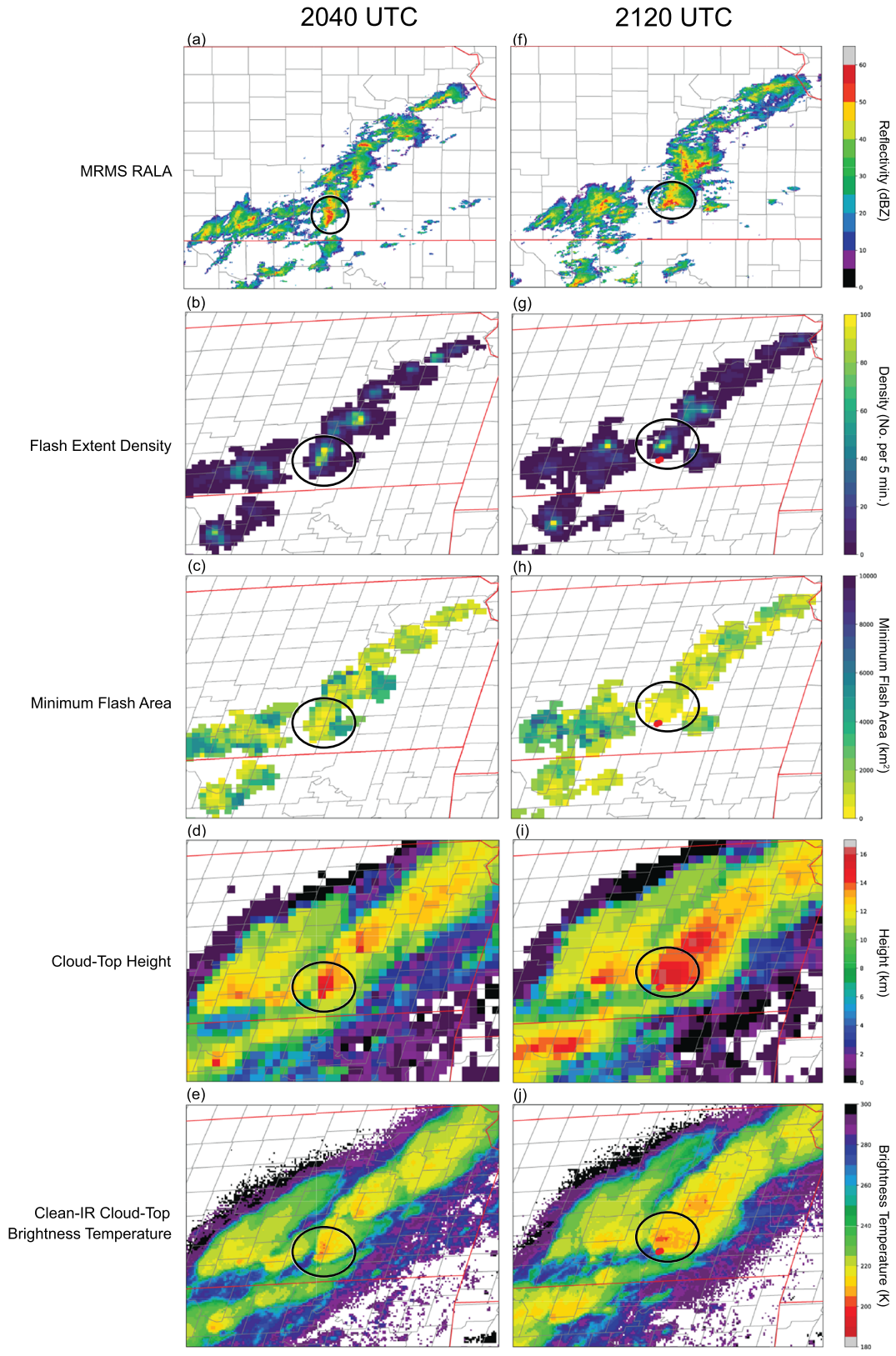

Figure 4. Snapshots from the 24 May 2019 case study at 2040 and 2120 UTC of MRMS RALA (a, f), FED (b, g), MFA (c, h), cloud-top height (d, i), and clean-IR cloud-top brightness temperature (e, j). Red, green, and blue dots represent the selected tornado, hail, and wind LSRs, respectively, over the previous 5 min. The black ellipse highlights to thunderstorm of study.

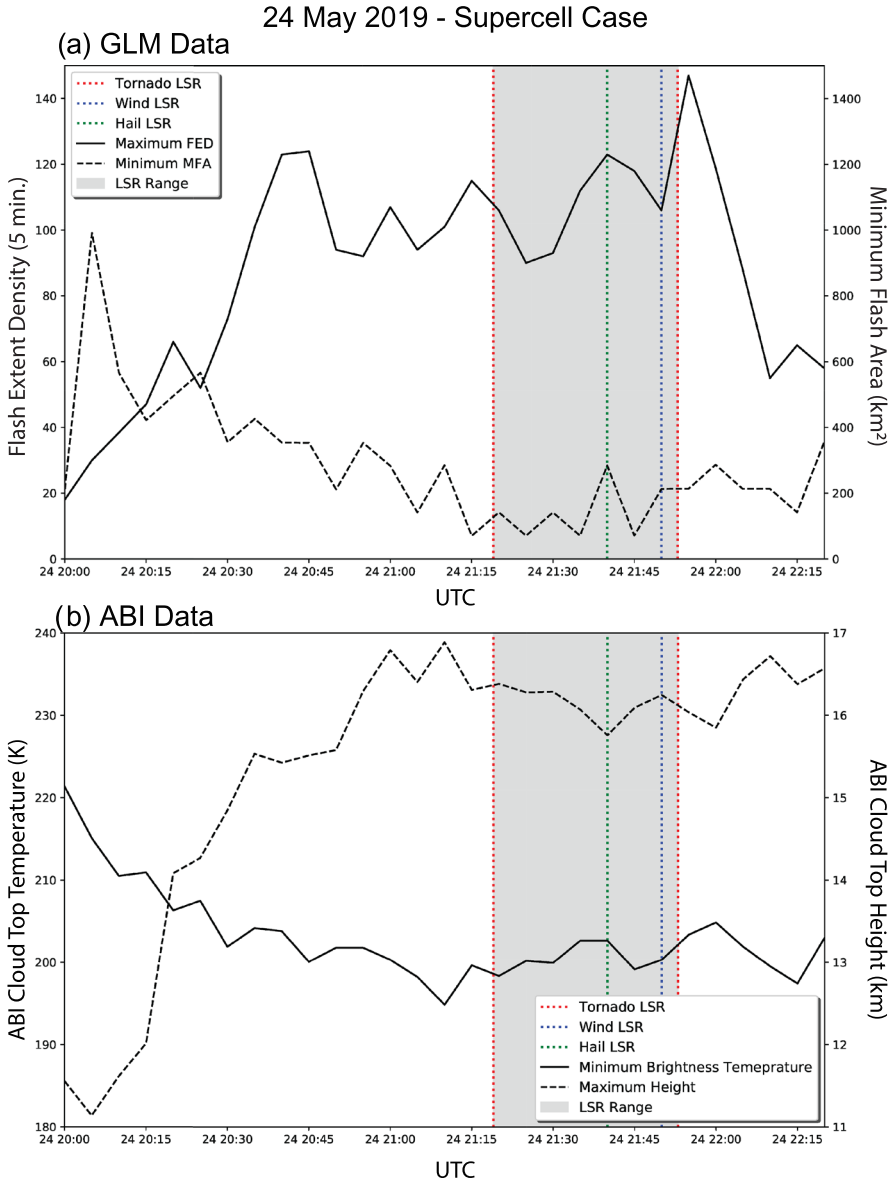

Figure 5. Time series of the 24 May 2019 supercell case with respect to its sampled maxima and minima in GLM (a) and ABI (b) variables over the entire storm. Panel (a) represents the maximum FED and minimum MFA, and panel (b) represents the maximum cloud-top height and minimum cloud-top brightness temperature. Red, green, and blue lines represent tornado, hail, and wind LSRs associated with the supercells, respectively, with the gray shaded region representing the time between the first and last LSR.

and growing upscale into a QLCS. By 2300 UTC, this transition was readily observed in the ABI and GLM data with regions of FED greater than 60 flashes per 5 min and MFA below 1,000 km^2, developing along the leading convective edge of the QLCS characterized by cloud-top heights exceeding 16 km and brightness temperatures below 205 K. Large regions of lower FED (<10 flashes per 5 min) and MFA larger than 4,000 km^2 (exceeding the 99th percentile) were observed in more stratified precipitation regions of the QLCS, with cloud-top brightness temperatures up to 10 K warmer than the QLCS convective core.

3.4.2. QLCS Case - 26–27 May 2019

A deep, longwave trough to the west of Kansas along with an intense midlevel shortwave trough moving quickly out of New Mexico on 26–27 May 2019 provided the instability for upscale growth of storms into a QLCS with a large-scale bow echo that produced damaging wind across wide areas of central Kansas. Convection first developed along the dry line in eastern New Mexico and grew upscale as it moved into the Texas and Oklahoma panhandles and across Kansas and northern Oklahoma overnight (26–27 May 2019).

Throughout the day on 26 May 2019, a frontal boundary propagated northward continuing southerly flow across all of the Southern and Central Plains. A dry line extended southward from the frontal boundary into southeast Colorado and across eastern New Mexico on the 1200 UTC surface analysis. Soundings from NWS Dodge City, KS at 1200 UTC on 26 May also show an environment with strong deep-layer shear supportive of supercell storms. CI occurred by 1700 UTC across southeast Colorado near the axis of the warm front and dry line. Storms continued to develop along the front and progress northeast, producing multiple hail and tornado reports across eastern Colorado through 0100 UTC on 27 May.

To the south, the diurnally forced dry line in New Mexico began to advance eastward, helping to initiate an organized line of thunderstorms by 2300 UTC on 26 May. The thunderstorms continued eastward, developing into a severe QLCS across the Oklahoma and Texas panhandles around 0300 UTC. MRMS RALA at 0300 UTC show the leading convective precipitation region exceeding 40 dBZ with several stronger cells exceeding 50 dBZ. These stronger convective cells in the QLCS were collocated with local maxima in GLM FED up to 84 flashes per 5 min, and MFA of 358 km^2(Figure 6a). Cloud-top heights across the Oklahoma and Texas panhandles consistently reached above 14 km along the convective precipitation region. Cloud-top brightness temperatures colder than 215 K were consistently observed along the convective precipitation region (Figure 6b), with minima of 201 K coinciding with the previously mentioned maxima in FED. This brightness temperature minima was below the 5th percentile of all samples within the larger 7-week study, while the highest cloud-top heights exceeded the 90th percentile. By 0330 UTC the maximum FED in the leading convective region increased to 124 flashes per 5 min, which exceeded the 97th percentile of all FED samples. From 0300 to 0400 UTC, the strongest cells embedded within the line were depicted by the highest FED values and coldest cloud-top temperatures and were consistently collocated with tornado and wind LSRs as the QLCS developed further across western Kansas. At 0345 UTC, four FED maxima exceeded 60 flashes per 5 min, while the MFA minima at these locations remained below 500 km^2, and the corresponding minima in cloud-top brightness temperatures below 205 K (Figures 7a–7e). These four regions were all associated with MRMS RALA above 50 dBZ, and values from both the GLM and ABI continued to highlight portions of the QLCS with enhanced updrafts capable of producing severe weather. When compared to the total population of all sampled cloud tops near an LSR, the ABI values were within the highest density region of samples from Figure 3a, while FED and MFA relationships from Figures 3b and 3c are also easily observed.

A large-scale bow-echo signature formed as the rear-inflow jet intensified at 700 hPa as the system moved across central Kansas through 0540 UTC (Figures 7f–7j). MRMS RALA values exceeded 50 dBZ in the leading convective precipitation region, coinciding with localized FED maxima decreased to approximately 65 flashes per 5 min across the convective region of the QLCS. Cloud-top brightness temperatures across central Kansas, however, continued to decrease with minima of 200 K and coincide with the region of highest reflectivity where two wind reports were located. A larger trailing stratiform precipitation region with reflectivities above 25 dBZ had also developed by this time. This region of the thunderstorm complex uniquely contained large MFA values greater than 7,000 km^2 with FED values below 10 flashes per 5 min but still maintained cloud-top heights between 12 and 14 km and brightness temperatures colder than 220 K. These horizontally expansive flashes indicated that even though the convective precipitation region and its associated hazards may have impacted the area hours ago in this case, the threat of lightning remained elevated as its own hazard.

4. Discussion

4.1. Cloud-Top Characteristics of Convection

The ACHA and CMIP variables provide additional context of the cloud structure and intensity of convection to GLM events measurements. This study considered whether the distributions of the gridded GLM imagery, ABI cloud-top height, and ABI brightness temperature distributions vary spatially as a function of their viewing angle elevations and if so, if the relationships between them were modified as well. Results from Figure 1b show clear differences in cloud-top height distributions as a function of viewing angle elevation. The most obvious relationship is the increasing bimodal distribution with increasing viewing angle elevation for nonflash locations (see the green violin plots in Figure 1b). This can largely be explained spatially as meteorological phenomena. As the viewing angle moves closer to nadir (>50°) there is an overwhelming shift in coverage from land to ocean regions, which coincides with the largest interquartile ranges as an effect of the bimodal distributions. This effect may be caused by regime changes in cloud-top heights, with

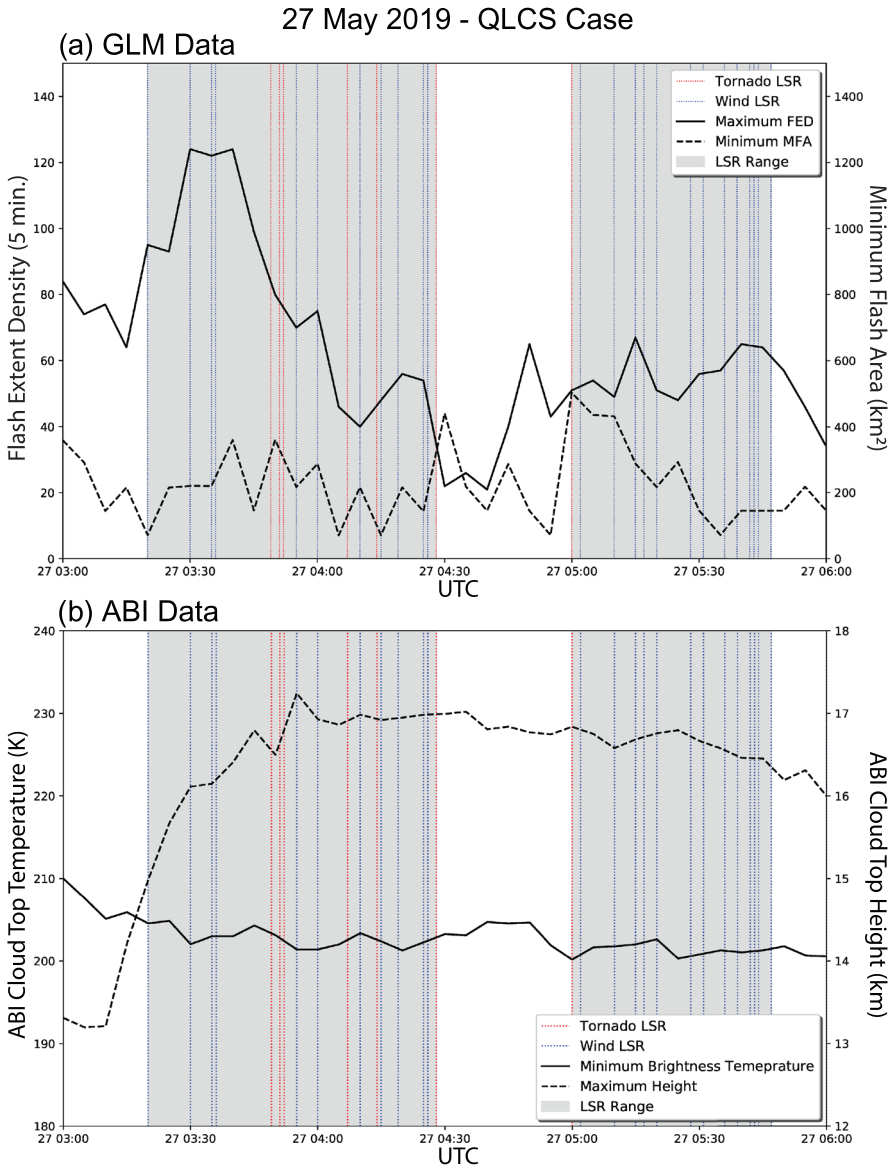

Figure 6. Time series of the 27 May 2019 QLCS case with respect to its sampled maxima and minima in GLM (a) and ABI (b) variables over the leading convective precipitation region. Panel (a) represents the maximum FED and minimum MFA, and panel (b) represents the maximum cloud-top height and minimum cloud-top brightness temperature. Red, green, and blue lines represent tornado, hail, and wind LSRs associated with the supercells, respectively, with the gray shaded region representing the time between the first and last LSR.

reduced synoptic scale forcing to generate ascent between 4 and 8 km. Cloud-top height observations from satellite lidar over the tropical Pacific by Palm et al. (2005) have revealed strong preferences in oceanic cloud-top heights to cirrus and boundary layer cumulus clouds. Their distributions were strikingly similar to those studied from cloud tops without GLM data in Figure 1b at viewing angle elevations greater than 50°. A notable decrease exists in the distribution of the cloud-top heights coincident with increasing values of the brightness temperatures at the lowest viewing angle elevations (Figure 1). These two trends would initially suggest that the ABI observes lower cloud-top heights and warmer brightness temperatures at the edges of its field of view. However, this feature may be driven by spatial trends in thunderstorm climatology across the CONUS scene, due to the generalized northwest shift in sampling area with decreasing viewing angle elevation.

Previous work has highlighted the caveats of utilizing cloud-top heights to assess lightning production. Price and Rind (1992) developed a simple lightning parameterization from theory and observations by Williams

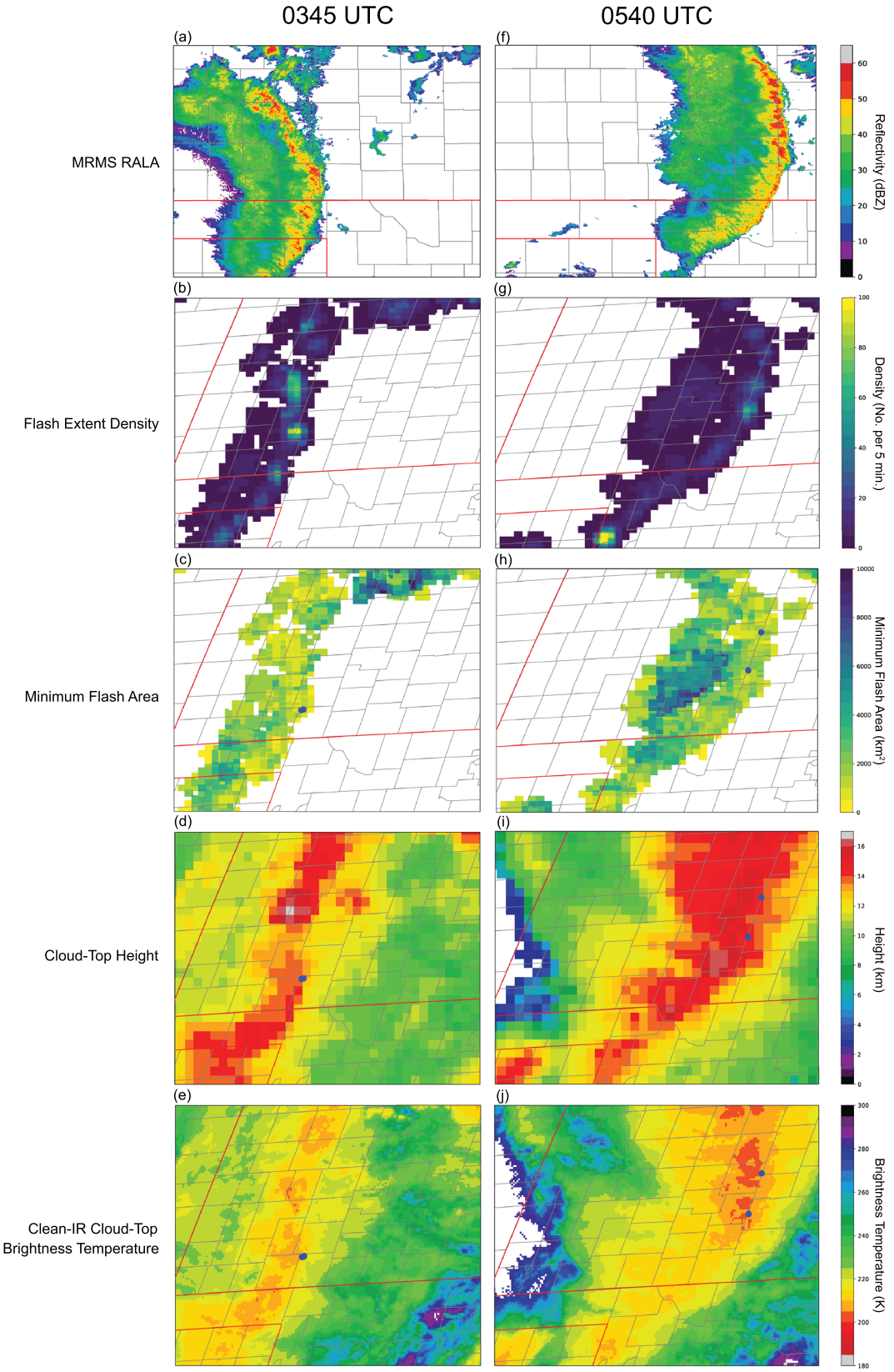

Figure 7. Snapshots from the 27 May 2019 case study at 0345 and 0540 UTC of MRMS RALA (a, f), FED (b, g), MFA (c, h), cloud-top height (d, i), and clean-IR cloud-top brightness temperature (e, j). Red, green, and blue dots represent the selected tornado, hail, and wind LSRs respectively over the previous 5 min.

(1985) and utilized satellite-derived cloud-top heights to estimate global lightning production. When inverting the parameterization and instead using measured total lightning production, calculations produced unrealistic cloud-top heights and updraft vertical velocities (Boccippio, 2002). The theoretical inconsistencies in these results constrain the utility of cloud-top height beyond this simple parameterization to other theoretical thunderstorm mechanisms. In the context of this study, cloud-top height was less reliable as an indicator of lightning production when compared to cloud-top brightness temperature (Figures 1b and 1c). One limitation of this study was the inability to specify cloud tops that were associated with convection, meaning that high-altitude cirrus clouds were included in the data sets. This includes cases of high-altitude cirrus above convection with lower cloud tops and may help to explain the sample of cloud tops exceeding 10 km at brightness temperatures above 240 K from Figure 2a.

One of the most prominent differences between the cloud tops that contained GLM flashes against cloud tops that did not contain GLM data was with the clean-IR brightness temperatures from Figure 1. While it is commonly understood that the stronger convective updrafts with sufficient rates of glaciation are more likely to produce lightning, the distributions of brightness temperatures show a clear shift below 240 K to the cloud tops associated with lightning. While cloud tops below freezing (273 K) can represent a shift in phase to ice, Figure 1c shows that the simple shift in phase is insufficient as an indicator of potential lightning production, as larger regions of charge must be present to generate electric fields conducive to lightning. Mohr et al. (1996) related brightness temperatures to cloud-to-ground lightning activity in the southern plains and found that flashes were most often coincident with temperatures between 210 and 250 K, further supporting the GLM observations of total lightning. In the context of mesoscale convective systems (MCSs), the fastest rates of growth of the IR cloud shield at 221 K tended to have higher total flash rates (Makowski et al., 2013). However, the minimum IR-brightness temperature from the MCSs was not as consistent for indicating total flash rates. Observations from the 27 May 2019 QLCS case study (Figure 6) support these results, even though the maximum FED values sampled along the leading convective region are not fully representative of total flash rate with respect to the larger spatial domains of MCSs.

The gridded GLM variables showed variations relative to their binned viewing angle elevation distributions, but multiple considerations of the GLM data are key to understanding why. The smallest FED values were observed at the greatest (70° to 80°) and least (20° to 30°) viewing angle elevations based upon their distributions (Figure 1d), but the reasons for these reduced values vary. The 70° to 80° viewing angle elevation region is by far the smallest and lowest average latitude of any other bin (Figure 1a) due to its proximity to nadir. The number of cloud-tops pixels producing lightning is therefore reduced to only 5,963, which represents approximately 0.01% of all 4.6 million flash locations within the data set. This region in the CONUS domain also contains no land, and when combined with its low latitude, means that this region has little synoptic or orographic forcing to produce strong thunderstorms. In contrast, the 20° to 30° viewing angle elevation region is almost entirely land based. However, its location in the northwest United States leads to the reduced climatological frequency and severity of thunderstorms as previously mentioned. GLM observations from the spring of 2018 by Rudlosky et al. (2019) coincide spatially with the reduced FED values. Similarly, Murphy and Said (2020) reported that the DE of GLM flashes drops off within 2,000 km of the edge of the field of view. From GOES-16 the effect is most pronounced in the northwestern United States (Bateman & Mach, 2020) and in our study would most greatly impact data in the 20° to 40° bins. However, without comparisons from ground-based sources such as those used by Bateman and Mach (2020), the true effect of reduced detection efficiencies at these lower viewing angle elevations for this study is unknown.

4.2. ABI-GLM Interrelationships

The three-dimensional scatter plots in Figures 2 and 3 were used to determine the trends in flash size and rate relative to their associated cloud-top characteristics. From Figure 2 it was observed qualitatively that with higher and colder cloud tops, FED generally increased while the MFA decreased. Conversely, lower and warmer cloud tops favored fewer FED and larger MFA. When reviewing the LSR-sampled data in Figure 3, these trends were more apparent, signaling that the more robust updrafts associated with severe convection provided a more focused view of convection and their associated ABI and GLM measurements. The three-dimensional scatter plots from Figures 2 and 3 provided a qualitative view of the inverse GLM flash size-rate relationship, but as previously mentioned limitations in sample size and variations in tightly clustered values made drawing definitive conclusions more difficult. Therefore, Figures 2d and 2e, along with Figures 3d and 3e, were created for a quantitative approach. Trends in the binned, median values from both

FED and MFA show a clear relationship with the highest and coldest cloud top coinciding with the most frequent and smallest flashes.

These observations come with the understanding that the GLM LCFA does not have the ability to cluster extremely large flashes due to the algorithm running in real time (Peterson, 2019). Over 3% of all GLM flashes exceed the LCFA-specified maximum group threshold, and the largest observed GLM flashes have been truncated below 10,000 km^2 prior to the Level 2 algorithm processing. The artificial termination of these more complex flashes is mostly observed with thunderstorms of high total flash rates exceeding 40 per minute (Mach, 2020). Even with these considerations, the relationships observed in this study are still consistent with the theory and observations presented in Bruning and MacGorman (2013) and Schultz et al. (2015) and highlight the utility of the GLM to capture this important relationship for convective nowcasting in NWS offices. Additionally, the identified flash size-rate relationship of the GLM gridded products with respect to cloud-top height and temperature supports work reported in Calhoun (2019) of a GLM-infrared (GLMIR) RGB product. This multiproduct and multisensor approach fully exploits the direct comparisons that can be made between the two sensors using glmtools while also providing this relationship in a compact single-product format. The GLMIR-RGB product in testing used the 10.3 μm clean-IR band, the same as this study. A notable shift in the distributions between all flash and nonflash locations is present (Figure 1c), supporting this multiproduct and multisensor approach to identify and monitor convection.

One application of this multisensor approach was the creation of a filter to remove GLM data that was associated with ocean glint. The ABI-GLM filter removed 10,763 pixels from the study with cloud-top heights less than 4 km, brightness temperatures above 270 K, and FED greater than 10 per 5 min. Spatially, the removed pixels were most often located in the CCD subarray east of the Bahamas, with other points scattered among the Gulf of Mexico, Caribbean, and the western Atlantic coast of the United States. Temporally pixels were frequently removed between 1500 and 2100 UTC each day, which coincide with periods of increased ocean glint. Bateman and Mach (2020) support these findings with higher rates of GLM FAR during the daytime across many of the same regions where flashes were removed. Both factors therefore suggest that the ABI-GLM filter removed almost entirely false GLM flash detections. However, false detections may still be included within the data set due to the limitation of the ABI-GLM variables themselves. Instances of ocean glint may be kept due to sporadic errors in the ACHA or measuring the heights of high-altitude cirrus clouds above these locations. Both of which would create cloud-top heights which exceed those specified in the filter. To complicate matters further, these artifacts may not exist in the current GLM data due to upgrades in ground processing in July 2019 to remove ocean glint and adjust the sensitivity of the CCD subarray boundaries.

The 24 May 2019 supercell case also supports the previously described relationships between ABI and GLM variables, especially during periods of intensification. The time series plot for the supercell case (Figure 5) showed a period of steadily increasing maximum FED values between 2010 and 2040 UTC from 38 to 124 flashes per 5 min, with cloud-top heights also increased during this period from 11 to 15 km. After this period of increase both values began to level off, however, cloud-top brightness temperature and MFA values continued to decrease until the first LSR associated with storm at 2119 UTC. When compared to the overall distribution of the 7-week study, the coldest and highest cloud tops in this case were representative of a thunderstorm capable of producing severe weather when the highest flash rates and smallest-possible flash sizes were also present.

In the 27 May 2019 case this relationship is not as well defined but presents a unique view of the QLCS as it evolves. Maximum FED counts in the leading convective precipitation region surged to a peak at 0330 UTC of 124 flashes per 5 min and the continued to decrease to 40 flashes per 5 min by 0410 (Figure 6). Minimum MFA sizes and cloud-top brightness temperatures during this period fluctuated between 71 to 360 km^2 and 201 to 203 K, respectively. During first half of the case, convection along the leading convective precipitation region was primary cellular, observed by localized maxima in MRMS RALA and GLM FED at 0345 UTC (Figures 7a and 7b). From 0345 to 0430 UTC, six tornado and eight wind LSRs are associated with this same region (Figure 6). The second half of this case, however, paints a different picture. Maximum FED counts along the convective line were consistently between 49 and 65 flashes per 5 min from 0500 to 0550 UTC, while cloud-top heights and brightness temperature ranged from 16 to 17 km and 200 to 201 K, respectively. While this steady state of lower maximum FED counts may signal a reduced severity of the QLCS, this time period also produced 1 tornado and 13 wind LSRs. Maximum MRMS RALA and GLM FED were also spread

more uniformly over the bow-echo signature observed at 0540 UTC (Figures 7f and 7g). The increased presence of the rear inflow jet as the QLCS developed is evident as it shifted from cellular to uniform convection along its leading edge. This corroborates with the shift in the distribution of tornado and wind LSRs and observations of the GLM and ABI variables. Even though the previously defined GLM-ABI relationships for the 24 May 2019 supercell case were not readily observed, the application of the combined data sources can be used to identify key changes in thunderstorm morphology and associated hazards.

4.3. Overshooting Tops

One of the observations when studying ABI-GLM data performance with respect to LSRs was a secondary axis of much larger increases in cloud-top heights with decreasing cloud-top brightness temperatures, above approximately 15 km (Figure 3). This feature is considerably less notable when examining the entire ABI-GLM data set (Figure 2), suggesting that convection with robust updrafts with the ability to produce severe weather is required to produce it. Although the ACHA does produce cloud-top temperature estimations for the full disk scene at 2 km, comparisons of these data to NWP temperature profiles may introduce errors in height estimations of up to 0.5 km (Heidinger, 2013). In reference to this study, errors may artificially inflate cloud-top height calculations in cases of rapidly intensifying updrafts, creating high cloud-top heights with comparatively warmer cloud-top brightness temperatures. While errors in the lower-resolution cloud-top height estimations are possible, the secondary axis extends well beyond the specified error range with heights up to 17.5 km. Cloud-top heights in the secondary axis of up to 2.5 km higher when compared to heights in the primary axis suggests it is in fact a physical process that is observed by the ABI.

The most reasonable explanation for this signature is the overshooting tops of convective updrafts, as mixing of adiabatically cooled air with the warmer ambient air above the tropopause creates higher cloud-top heights with warmer brightness temperatures relative to those observed in the primary cloud-top height and brightness temperature axis. Connections between overshooting tops and severe convective phenomena such as large hail, damaging winds, and tornadoes (Dworak et al., 2012; Fujita, 1989; Negri & Adler, 1981; Reynolds, 1980) therefore support the observed secondary axis in Figure 3. Overshooting tops have also been linked to an observed IR satellite signature called an enhanced-V representative of an above anvil cirrus plume (Homeyer, 2014; McCann, 1983). In this case, a region of warmer IR brightness temperatures is observed downshear from a temperature minimum associated with the overshooting top due to the injection of convective material into the lower stratosphere, therefore, modifying its chemistry and radiation budget (Anderson et al., 2012). Due to the relatively short lifetime of convective overshooting events (Dworak et al., 2012; Solomon et al., 2016), the 5-min resolution of all ABI CONUS products allows for further study of these events with respect to total lightning production by the GLM. In this study the secondary axis is solely representative of the overshooting tops and does not delineate between overshooting tops that do produce above anvil cirrus plumes and those that do not. Observations of above anvil cirrus plumes using the ACHA have shown deficiencies in accurately estimating cloud-top height. The warmer cloud-top temperature estimations from the plume itself produce lower heights due to its dependence on model-derived temperature profiles to generate the product.

5. Summary and Conclusions

Seven weeks of ABI and GLM data were analyzed from April–May 2019 across the GOES-16 CONUS domain. Direct comparisons between the gridded GLM imagery from glmtools (FED and MFA) and the ABI-derived cloud-top heights and clean-IR brightness temperatures were made by compositing all GLM data for each scan and using a spatial selective-sampling method with a horizontal resolution of 20 km. The results were composed of over 4.6 million data points containing ABI and GLM data and 2 million randomly sampled data points where clouds were present in the ABI data but lightning was not detected from the GLM. Case studies from 24 May 2019 of a supercell and 27 May 2019 of a QLCS were also studied to support and reveal variations of observed relationships from the 7-week study.

The overarching conclusion from this study is that the combination of ABI data and GLM data provides complementary insight into thunderstorm morphology and meaningful lightning interrelationships with evolving storm characteristics. Inverse relationships between flash rate and flash size were observed in both the bulk study and cases of discrete convection, consistent with previous studies. Further support for this conclusion was provided by observations of MFA in cases of high FED (greater than 24 flashes per 5 min) and in proximity to LSRs. Data from near LSR locations revealed the presence of overshooting tops, a consistent

indicator of robust updrafts capable of producing severe weather. These stronger storms were associated with higher FED at the colder, higher cloud tops and a greater frequency of smaller flash sizes.

Another important result is the notable differences between IR cloud-top brightness temperatures at locations containing lightning flashes when compared against samples without flashes. Specifically, brightness temperatures colder than 240 K favored cloud tops, which coincide with lightning production, signaling the products ability to identify and monitor convection with potential thresholds. The observed viewing angles of convection also revealed spatial variations across the CONUS scene, particularly on measurable cloud-top heights from the ACHA GOES algorithm. The difference in distributions for ABI cloud-top brightness temperature was maximized for viewing angle elevations above 40°. This work supports the use of the clean-IR brightness temperature CMIP for the GLMIR-RGB product and encourages future development for NWS operations.

While this study uses a satellite-to-satellite comparison, focusing solely on cloud-top features, future studies using parallax-corrected data from glmtools would allow comparisons with other remote sensing systems such as radar, ground-based LLS, and surface observations. With the ability to make these kinds of direct comparisons, in-cloud properties and processes can be related to thunderstorm electrodynamics through their relative flash characteristics. Vertically integrated radar variables specifically may provide keys to the optical properties of the thunderstorm, to further understand variations in GLM flash characteristics and DE.

Data Availability Statement

The ABI and GLM data used in this study can be accessed from the NOAA CLASS service (https://www.class.noaa.gov/), Google Cloud (https://console.cloud.google.com/marketplace/partners/noaa-public), Amazon Web Services (https://registry.opendata.aws/noaa-goes/), or the GOES-16 Data Archive (https://goes16.metr.ou.edu/). Figures were created using Cartopy (Elson et al., 2018), Matplotlib (Hunter, 2007), and Seaborn (Waskom et al., 2020).

Acknowledgments
Funding for this work was provided by the NOAA/NESDIS Office of Projects, Planning and Analysis GOES-R Reduction program under Grant NA16OAR4320115. The authors would like to thank Dr. Eric Bruning for his assistance in configuring the glmtools software package (Bruning, 2019) and fruitful discussion throughout the project, along with three anonymous reviewers for their insightful feedback and discussion of the manuscript.

References

Allen, J. T., & Tippett, M. K. (2015). The characteristics of United States hail reports: 1955–2014. *Electronic Journal of Severe Storms Meteorology*, *10*, 31.

Anderson, J. G., Wilmouth, D. M., Smith, J. B., & Sayres, D. S. (2012). UV dosage levels in summer: Increased risk of ozone loss from convectively injected water vapor. *Science*, *337*(6096), 835–839. https://doi.org/10.1126/science.1222978

Bateman, M., & Mach, D. (2020). Preliminary detection efficiency and false alarm rate assessment of the Geostationary Lightning Mapper on the GOES-16 satellite. *Journal of Applied Remote Sensing*, *14*(03), 1. https://doi.org/10.1117/1.JRS.14.032406.full

Boccippio, D. J. (2002). Lightning scaling relations revisited. *Journal of the Atmospheric Sciences*, *59*, 19. https://doi.org/10.1175/1520-0469(2002)059<1086:LSRR>2.0CO;2

Bruning, E. C. (2019). glmtools. https://doi.org/10.5281/zenodo.2648658

Bruning, E. C., & MacGorman, D. R. (2013). Theory and observations of controls on lightning flash size spectra. *Journal of the Atmospheric Sciences*, *70*(12), 4012–4029. https://doi.org/10.1175/JAS-D-12-0289.1

Bruning, E. C., Tillier, C. E., Edgington, S. F., Rudlosky, S. D., Zajic, J., Gravelle, C., et al. (2019). Meteorological imagery for the geostationary lightning mapper. *Journal of Geophysical Research: Atmospheres*, *124*, 14,285–14,309. https://doi.org/10.1029/2019JD030874

Calhoun, K. M. (2018). Feedback and recommendations for the Geostationary Lightning Mapper (GLM) in severe and hazardous weather forecasting and warning operations: GOES Proving Ground.

Calhoun, K. M. (2019). Feedback and recommendations for the Geostationary Lightning Mapper (GLM) in severe and hazardous weather forecasting and warning operations: GOES Proving Ground.

Calhoun, K. M., Bruning, E. C., & Schultz, C. J. (2018). Principles and operational applications of Geostationary Lightning Mapper data for severe and local storms. Stowe, VT.

Calhoun, K. M., MacGorman, D. R., Ziegler, C. L., & Biggerstaff, M. I. (2013). Evolution of lightning activity and storm charge relative to dual-Doppler analysis of a high-precipitation supercell storm. *Monthly Weather Review*, *141*(7), 2199–2223. https://doi.org/10.1175/MWR-D-12-00258.1

Calhoun, K. M., Mansell, E. R., MacGorman, D. R., & Dowell, D. C. (2014). Numerical simulations of lightning and storm charge of the 29 May 2004 Geary, Oklahoma, supercell thunderstorm using EnKF mobile radar data assimilation. *Monthly Weather Review*, *142*(11), 3977–3997. https://doi.org/10.1175/MWR-D-13-00403.1

Cummins, K. L., & Murphy, M. J. (2009). An overview of lightning locating systems: History, techniques, and data uses, with an in-depth look at the U.S. NLDN. *IEEE Transactions on Electromagnetic Compatibility*, *51*(3), 499–518. https://doi.org/10.1109/TEMC.2009.2023450

Curran, E. B., Holle, R. L., & Lpez, R. E. (2000). Lightning casualties and damages in the United States from 1959 to 1994. *Journal of Climate*, *13*(19), 3448–3464. https://doi.org/10.1175/1520-0442%282000%29013%3C3448%3ALCADIT%3E2.0

Darden, C. B., Nadler, D. J., Carcione, B. C., Blakeslee, R. J., Stano, G. T., & Buechler, D. E. (2010). Utilizing total lightning information to diagnose convective trends. *Bulletin of the American Meteorological Society*, *91*(2), 167–176. https://doi.org/10.1175/2009BAMS2808.1

Dworak, R., Bedka, K., Brunner, J., & Feltz, W. (2012). Comparison between GOES-12 overshooting-top detections, WSR-88D radar reflectivity, and severe storm reports. *Weather and Forecasting*, *27*(3), 684–699. https://doi.org/10.1175/WAF-D-11-00070.1

Edgington, S. F. (2020). Over a year on orbit with two lightning mappers: Lessons learned. Boston, MA. https://ams.confex.com/ams/2020Annual/meetingapp.cgi/Paper/368583

Elson, P., Andrade, E. S., Hattersley, R., Campbell, E., Dawson, A., May, R., et al. (2018). SciTools/cartopy: v0.17.0. Zenodo, https://doi.org/10.5281/zenodo.1490296

Emersic, C., & Saunders, C. P. R. (2010). Further laboratory investigations into the relative diffusional growth rate theory of thunderstorm electrification. *Atmospheric Research*, *98*(2-4), 327–340. https://doi.org/10.1016/j.atmosres.2010.07.011

Fujita, T. T. (1989). The Teton-Yellowstone Tornado of 21 July 1987. *Monthly Weather Review*, *117*, 1913–1940. https://doi.org/10.1175/1520-0493(1989)117<1913:TTYTOJ>2.0.CO;2

Goodman, S. J., Blakeslee, R. J., Koshak, W. J., Mach, D., Bailey, J., Buechler, D., et al. (2013). The GOES-R Geostationary Lightning Mapper (GLM). *Atmospheric Research*, *125-126*, 34–49. https://doi.org/10.1016/j.atmosres.2013.01.006

Goodman, S. J., Mach, D., Koshak, W., & Blakeslee, R. (2012). GLM lightning cluster-filter algorithm. NOAA/NESDIS. https://www.star.nesdis.noaa.gov/goesr/documents/ATBDs/Baseline/ATBD_GOES-R_GLM_v3.0_Jul2012.pdf

Heidinger, A. (2013). Algorithm theoretical basis document ABI cloud height. NOAA/NESDIS. https://www.star.nesdis.noaa.gov/goesr/docs/ATBD/Cloud_Height.pdf

Homeyer, C. R. (2014). Formation of the enhanced-V infrared cloud-top feature from high-resolution three-dimensional radar observations. *Journal of the Atmospheric Sciences*, *71*(1), 332–348. https://doi.org/10.1175/JAS-D-13-079.1

Hunter, J. D. (2007). Matplotlib: A 2D graphics environment. *Computing in Science Engineering*, *9*(3), 90–95. https://doi.org/10.1109/MCSE.2007.55

Jensenius, J. J. Jr. (2019). A detailed analysis of lightning deaths in the United States from 2006 through 2019. National Lightning Safety Council, https://www.weather.gov/media/safety/Analysis06-18.pdf

Kelly, D. L., Schaefer, J. T., & Doswell, C. A. (1985). Climatology of nontornadic severe thunderstorm events in the United States. *Monthly Weather Review*, *113*, 1997–2014. https://doi.org/10.1175/1520-0493(1985)113<1997:CONSTE>2.0.CO;2

MacGorman, D. R., Few, A. A., & Teer, T. L. (1981). Layered lightning activity. *Journal of Geophysical Research*, *86*(C10), 9900. https://doi.org/10.1029/JC086iC10p09900

MacGorman, D. R., & Rust, W. D. (1998). *The electrical nature of storms* (1st ed.). Oxford: Oxford University Press.

Mach, D. M. (2020). Geostationary Lightning Mapper clustering algorithm stability. *Journal of Geophysical Research: Atmospheres*, *125*, e2019JD031900. https://doi.org/10.1029/2019JD031900

Makowski, J. A., MacGorman, D. R., Biggerstaff, M. I., & Beasley, W. H. (2013). Total lightning characteristics relative to radar and satellite observations of Oklahoma mesoscale convective systems. *Monthly Weather Review*, *141*(5), 1593–1611. https://doi.org/10.1175/MWR-D-11-00268.1

Mansell, E. R., MacGorman, D. R., Ziegler, C. L., & Straka, J. M. (2005). Charge structure and lightning sensitivity in a simulated multicell thunderstorm. *Journal of Geophysical Research*, *110*, D12101. https://doi.org/10.1029/2004JD005287

McCann, D. W. (1983). The enhanced-V: A satellite observable severe storm signature. *Monthly Weather Review*, *111*(1), 887–894. https://doi.org/10.1175/1520-0493(1983)111<0887:TEVASO>2.0.CO;2

Mecikalski, R. M., & Carey, L. D. (2018). Radar reflectivity and altitude distributions of lightning flashes as a function of three main storm types. *Journal of Geophysical Research: Atmospheres*, *123*, 12,814–12,828. https://doi.org/10.1029/2018JD029238

Mohr, K. I., Toracinta, E. R., Zisper, E. J., & Orville, R. E. (1996). A comparison of WSR-88D reflectivities, SSM/I brightness temperatures, and lightning for mesoscale convective systems in Texas. Part I: Radar reflectivity and lightning. *Journal of Applied Meteorology*, *35*, 919–931. https://doi.org/10.1175/1520-0450(1996)035<0902:ACOWRS>2.0.CO;2

Murphy, M. J., & Said, R. K. (2020). Comparisons of lightning rates and properties from the U.S. National Lightning Detection Network (NLDN) and GLD360 with GOES Geostationary Lightning Mapper and advanced baseline imager data. *Journal of Geophysical Research: Atmospheres*, *125*, e2019JD031172. https://doi.org/10.1029/2019JD031172

Negri, A. J., & Adler, R. F. (1981). Relation of satellite-based thunderstorm intensity to radar-estimated rainfall. *Journal of Applied Meteorology*, *20*, 288–300. https://doi.org/10.1175/WAF-D-11-00070.1

Palm, S. P., Benedetti, A., & Spinhirne, J. (2005). Validation of ECMWF global forecast model parameters using GLAS atmospheric channel measurements: Model validation using glas data. *Geophysical Research Letters*, *32*, L22S09. https://doi.org/10.1029/2005GL023535

Peterson, M. (2019). Research applications for the geostationary lightning mapper operational lightning flash data product. *Journal of Geophysical Research: Atmospheres*, *124*, 10,205–10,231. https://doi.org/10.1029/2019JD031054

Potvin, C. K., Broyles, C., Skinner, P. S., Brooks, H. E., & Rasmussen, E. (2019). A Bayesian hierarchical modeling framework for correcting reporting bias in the U.S. Tornado database. *Weather and Forecasting*, *34*(1), 15–30. https://doi.org/10.1175/WAF-D-18-0137.1

Price, C., & Rind, D. (1992). A simple lightning parameterization for calculating global lightning distributions. *Journal of Geophysical Research*, *97*(D9), 9919–9933. https://doi.org/10.1029/92JD00719

Purdom, J. F. W. (1976). Some uses of high-resolution GOES imagery in the mesoscale forecasting of convection and its behavior. *Monthly Weather Review*, *104*, 1474–1483. https://doi.org/10.1175/1520-0493(1976)104<1474:SUOHRG>2.0.CO;2

Reynolds, D. W. (1980). Observations of damaging hailstorms from geosynchronous satellite digital data. *Monthly Weather Review*, *108*, 337–348. https://doi.org/10.1175/1520-0493(1980)108<0337:OODHFG>2.0.CO;2

Roberts, R. D., & Rutledge, S. (2003). Nowcasting storm initiation and growth using GOES-8 and WSR-88D data. *Weather and Forecasting*, *18*, 23. https://doi.org/10.1175/1520-0434(2003)018<0562:NSIAGU>2.0.CO;2

Rudlosky, S. D., & Armstrong, P. (2019). GLM ground system software status: Cooperative Institute for Climate and Satellite Studies-Maryland. https://lightning.umd.edu/documents/GS_Status/GLM_GS_Status_8_21_19.pdf

Rudlosky, S. D., Goodman, S. J., Virts, K. S., & Bruning, E. C. (2019). Initial Geostationary Lightning Mapper observations. *Geophysical Research Letters*, *46*, 1097–1104. https://doi.org/10.1029/2018GL081052

Schmit, T. J., Griffith, P., Gunshor, M. M., Daniels, J. M., Goodman, S. J., & Lebair, W. J. (2017). A closer look at the ABI on the GOES-R series. *Bulletin of the American Meteorological Society*, *98*(4), 681–698. https://doi.org/10.1175/BAMS-D-15-00230.1

Schmit, T. J., Gunshor, M., Fu, G., Rink, T., Bah, K., Zhang, W., & Wolf, W. (2012). GOES-R Advanced Baseline Imager (ABI) algorithm theoretical basis document for cloud and moisture imagery product (CMIP). NOAA/NESDIS.

Schultz, C. J., Carey, L. D., Schultz, E. V., & Blakeslee, R. J. (2015). Insight into the kinematic and microphysical processes that control lightning jumps. *Weather and Forecasting*, *30*(6), 1591–1621. https://doi.org/10.1175/WAF-D-14-00147.1

Schultz, C. J., Carey, L. D., Schultz, E. V., & Blakeslee, R. J. (2017). Kinematic and microphysical significance of lightning jumps versus nonjump increases in total flash rate. *Weather and Forecasting*, *32*(1), 275–288. https://doi.org/10.1175/WAF-D-15-0175.1

Schultz, C. J., Petersen, W. A., & Carey, L. D. (2009). Preliminary development and evaluation of lightning jump algorithms for the real-time detection of severe weather. *Journal of Applied Meteorology and Climatology*, *48*(12), 2543–2563. https://doi.org/10.1175/2009JAMC2237.1

Smith, T. M., Lakshmanan, V., Stumpf, G. J., Ortega, K. L., Hondl, K., Cooper, K., et al. (2016). Multi-radar multi-sensor (MRMS) severe weather and aviation products: Initial operating capabilities. *Bulletin of the American Meteorological Society*, *97*(9), 1617–1630. https://doi.org/10.1175/BAMS-D-14-00173.1

Soler, T., & Eisemann, D. W. (1994). Determination of look angles to geostationary communication satellites. *Journal of Surveying Engineering*, *120*(3), 115–127. https://doi.org/10.1061/%28ASCE%290733-9453%281994%29120%3A3%%28115%29

Solomon, D. L., Bowman, K. P., & Homeyer, C. R. (2016). Tropopause-penetrating convection from three-dimensional gridded NEXRAD data. *Journal of Applied Meteorology and Climatology*, *55*(2), 465–478. https://doi.org/10.1175/JAMC-D-15-0190.1

Takahashi, T. (1978). Riming electrification as a charge generation mechanism in thunderstorms. *Journal of the Atmospheric Sciences*, *35*, 1536–1548. https://doi.org/10.1175/1520-0469(1978)035<1536:REAACG>2.0.CO;2

Trapp, R. J., Wheatley, D. M., Atkins, N. T., Przybylinski, R. W., & Wolf, R. (2006). Buyer beware: Some words of caution on the use of severe wind reports in postevent assessment and research. *Weather and Forecasting*, *21*(3), 408–415. https://doi.org/10.1175/WAF925.1

Waskom, M., Botvinnik, O., Ostblom, J., Lukauskas, S., Hobson, P., MaozGelbart, et al. (2020). mwaskom/seaborn: v0.10.0 (January 2020). Zenodo, https://doi.org/10.5281/zenodo.3629446

Williams, E. R. (1985). Large-scale charge separation in thunderclouds. *Journal of Geophysical Research*, *90*(D4), 6013. https://doi.org/10.1029/JD090iD04p06013

Williams, E. R., Boldi, B., Matlin, A., Weber, M., Hodanish, S., Sharp, D., et al. (1999). The behavior of total lightning activity in severe Florida thunderstorms. *Atmospheric Research*, *51*(3-4), 245–265. https://doi.org/10.1016/S0169-8095(99)00011-3

Ziegler, C. L., & MacGorman, D. R. (1994). Observed lightning morphology relative to modeled space charge and electric field distributions in a tornadic storm. *Journal of the Atmospheric Sciences*, *51*(6), 833–851. https://doi.org/10.1175/1520-0469(1994)051<0833:OLMRTM>2.0.CO;2